RSC Advances

PAPER

View Article Online
View Journal | View Issue

Cite this: *RSC Adv.*, 2023, **13**, 28382

Enhanced anodic catalytic performance in $PrFeO_{3-\delta}$ of perovskite materials *via* Co-doping with Sr and VB subgroup metals (V, Nb, Ta)

Hongfei Chen, [a] Zhe Lü, *[a] Zhipeng Liu,[b] Yujie Wu,[a] Shuai Wang[a] and Zhihong Wang[a]

The anodic catalytic capability of $PrFeO_{3-\delta}$ is restricted by the Fe-site element type in the perovskite material structure due to its low electrical conductivity of electrons. Here, we present a strategy for tuning the Fe-site element type *via* Sr and VB subgroup metals (V, Nb, Ta) co-doping to enhance the anodic catalytic performance of $PrFeO_{3-\delta}$ anode materials. Our calculations show that Sr and Nb co-doping has suitable hydrogen adsorption energy for $PrFeO_{3-\delta}$ anode materials, and its adsorption energy is adjusted to −0.717 eV, which is more suitable to absorb the hydrogen molecule than other high-profile perovskite anode materials. Meanwhile, after the doped surface is adsorbed by hydrogen molecules, the bond length lengthens until it breaks, and one of the broken hydrogen atoms moves directly above the surface oxygen atom, which is beneficial for accelerating the anodic catalytic reaction. Thus, the $Pr_{0.5}Sr_{0.5}Fe_{0.875}Nb_{0.125}O_{3-\delta}$ material is a promising perovskite anode catalyst. Interestingly, the stability of $PrFeO_{3-\delta}$ is significantly affected by the oxygen vacancy content; the structural stability of the undoped system can be maintained *via* Sr and Nb co-doping to avoid decomposition, which provides new thinking to maintain the high stability of perovskite ferrite materials. Furthermore, we find that relative to the $PrFeO_{3-\delta}$, the $Pr_{0.5}Sr_{0.5}Fe_{0.875}Nb_{0.125}O_{3-\delta}$ surface of hydrogen adsorption has obvious charge transfer and upward shift of the d-band center. Our anodic catalytic theoretical work shows that Sr and Nb co-doping can effectively enhance the catalytic performance of the $PrFeO_{3-\delta}$ ferrite materials.

Received 25th July 2023
Accepted 18th September 2023

DOI: 10.1039/d3ra05026b

rsc.li/rsc-advances

1. Introduction

The fuel cell (FC) is one of the candidate energy conversion devices investigated for improving the efficiency of new energy conversion significantly. Since solid oxide fuel cell (SOFC) is shown to have a relatively excellent practical service life, long-term stability and fuel suitability, it is considered to be a third-generation FC with good development potential.[1–9] The following three procedures are included in the working process of SOFC. First, the cathode side gains electrons. Next, due to the concentration difference, oxygen ions move *via* the electrolyte to reach the anode. Finally, the generated electrons move back *via* an external circuit.[10,11]

Based on the working principle of SOFC, its various parts of the construction materials have been widely studied. Among them, the anode is the crucial component of SOFC with unique selection requirements, such as conductivity, stability, thermal expansion and catalytic capacity.[12,13] The anodes currently under study are mainly Ni-based, Cu–CeO_2-based and Perovskite and its derived structural systems. Ni-based systems are prevented from being used in the long term because of their instability and high cost.[14–16] An effective dry catalyst was prepared, which could effectively reduce the carbon resistance while increasing the power density by Yao *et al.*, which is very important to improve the efficiency of converting waste heat of biogas fuel into chemical energy.[17] Cheng *et al.* revealed the nanocrystalline properties of NiO-YSZ materials and used techniques to distinguish the distribution of NiO in microstructure from NiO and YSZ particles.[18] Cu is used to impede the deposition of carbon from Ni-based systems because it is hard to form C–C bonds in fuels. Nevertheless, Cu with agglomeration phenomenon is considered detrimental to anodic catalysis due to the high-temperature operation.[19] Jung *et al.* studied the effect of Cu distribution on wet hydrogen fuel *via* the impregnation method which made Cu distribution in anode uniform.[20] Ye *et al.* proposed a two-strip anode casting method, studied its performance characteristics in different fuels, and compared its long-term performance in high-temperature streams.[21]

The rise of anode material research makes people pay attention to perovskite materials. In recent years, perovskite and its derived structures play an important role in SOFC electrode research.[22–31] Perovskite and its derivative systems are used in classical cathode materials. $LaSr(MnO_3)_2$, as the

[a]*School of Physics, Harbin Institute of Technology, Harbin 150001, China. E-mail: lvzhe@hit.edu.cn*

[b]*Electric Power Research Institute, State Grid Heilongjiang Electric Power Company Ltd, Harbin 150030, China*

representative material of cathode, has good physical properties, cathode stability and electrode performance above 1000°.[32,33] Since the perovskite cathode materials, perovskite system anode has become a research hotspot with constantly being explored.[34–42] Cr-based perovskite is well regarded for reducing the gas electrode and maintaining excellent stability.[43–45] In particular, Fe-based perovskite has attracted extraordinary inquiry interest recently.[46] Perovskite materials have shown many advantages in anode applications.

Unfortunately, compared with Ni-based anode, perovskite anode $PrFeO_{3-\delta}$ has a low electronic conductivity that greatly restricts the anodic catalytic performance in the SOFC field.[47,48] Therefore, it's highly necessary to adopt a facile arrangement for improving the conductivity of materials to enhance the anodic catalytic performance. Fe-site doping is a frequent arrangement for tuning conductivity. Whereas, single doping usually causes more appearances of impurity defects that trigger more serious defect structure evolution.[49]

To overcome the low electronic conductivity issue, Sr and VB subgroup metals co-doping is a practical and facile arrangement to improve the electronic conductivity of $PrFeO_{3-\delta}$, thus promoting the anodic catalytic reaction. Doping with Nb elements helps to prevent the intrinsic material from decomposing and simultaneously forms Nb–O bonds to enhance the stability of the intrinsic structure. The co-doping with Sr elements, with their appropriate ion radius, can balance the valence state imbalance caused by higher-valent doping. Although there are rare reports on the stability and catalytic performance of $PrFeO_{3-\delta}$, many studies above improving the catalytic performance of perovskite electrodes by increasing the conductivity of Fe-site element have been reported. By comparing and investigating the doping, redox stability and conductivity of $LaCrO_3$, Jiang *et al.* calculated that A-site doping with few basic elements can reduce the activation energy of conductivity thus significantly improving the electrical conductivity.[50] Shin *et al.* calculated that the $PrMnO_3$ formation energy of oxygen vacancy is significantly reduced compared to that of a chalcogenide such as $LaMnO_3$. Oxygen adsorption on the surface of $LaMnO_3$ was investigated by theoretical simulations. Found that the oxygen vacancies in $La_{0.5}Sr_{0.5}FeO_{3-\delta}$ reduced the electrical conductivity, ultimately leading to a metal-to-semiconductor structural transition under low pressures.[51] However, calculations of Zhou display that the oxygen vacancy formation energy of $PrMnO_3$ is significantly reduced compared to that of a chalcogenide such as $LaMnO_3$.[52] Although some progress has been made in the experimental research and theoretical reports on perovskite anode materials.

To date, only rare studies above tuning the bulk formation energy, initial and final-state with surface adsorption of the $PrFeO_{3-\delta}$ anode *via* co-doping.[53,54] Nevertheless, in these reports, the initial and final-state adsorption surface is not calculated, which cannot fully further explain the mechanism of anode catalysis. With our current research, few details are regarded with the oxygen vacancy stability and adsorption mechanism of $PrFeO_{3-\delta}$ systems under Sr and Fe-site co-doping. From an experimental perspective, it is indeed possible to prepare the anode materials for this system. Among them, $Pr_{0.5}Sr_{0.5}FeO_3$, $Pr_{0.5}Sr_{0.5}Fe_{0.875}V_{0.125}O_3$, and $Pr_{0.5}Sr_{0.5}Fe_{0.875}Nb_{0.125}O_3$ powders were synthesized *via* the sol–gel method. $Pr_{0.5}Sr_{0.5}Fe_{0.875}Ta_{0.125}O_3$, on the other hand, was synthesized using the conventional solid–state reaction method.

In this theoretical calculation work, we focus on the bulk and surface of pristine and co-doping $PrFeO_{3-\delta}$ systems, such as bulk forming energy, oxygen vacancy formation energy and adsorption performance. We find that $PrFeO_{3-\delta}$ under Sr and Nb co-doped is a promising anode catalyst due to its desirable adsorption property value, significant charge transfer and d-band center moves upward. Meanwhile, the stability of the $PrFeO_{3-\delta}$ with different oxygen vacancy concentrations and sites is differ widely, which further illustrates the effect of oxygen vacancy from the structure of perovskite. Sr and Nb co-doped the adsorption property value of $PrFeO_{3-\delta}$ adjust to -0.717 eV, that neither the catalytic effect is strong enough, nor does it cause electrode poisoning. In addition, the structure of the final-states co-doped anode is conducive to the next catalytic step. Our simulated results manifest that Sr and Fe-site co-doped can effectively augment the anode catalytic performance of the $PrFeO_{3-\delta}$.

2. Calculation methods

The VASP code was executed through the whole simulated calculations.[55,56] The PAW can express the core–electron interaction, while the exchange and correction effects was adopted with the GGA-PBE.[57–59] The core–electron interaction refers to the interaction between the atomic nucleus and electrons. It arises from the Coulomb interaction, which is the interaction between charged particles. This interaction directly influences the motion, energy, and distribution of electrons, thereby determining the external behavior and chemical reactions of atoms. In all part simulated work, the cutoff energy and the energy convergence were tested to be 500 eV and 1.0×10^{-6} eV, separately. The vacuum layer was set to 20 Å thickness along the *z*-direction. The *k*-point mesh sampling for $PrFeO_{3-\delta}$ bulk and surface in the Brillouin zone was tested to $6 \times 6 \times 6$ and $6 \times 6 \times 1$, respectively. The force was set to 0.05 eV $Å^{-1}$. We adopt the DFT+U method, in which the U_{eff} $(=U-J)$ Hubbard parameter is added to the transition elements ($U_{Fe,d} = 5.3$ eV, $U_{V,d} = 5.3$ eV, $U_{Nb,d} = 5.0$ eV, and $U_{Ta,d} = 4.8$ eV), which was adopted in the previous study.[60–62] The maximum stress was set to 0.1 GPa. We calculated the formation energy according to

$$E_f = \frac{E(A_aB_bC_c) - aE(A) - bE(B) - cE(C)}{a+b+c} \quad (1)$$

where a and $E(A)$ are the number of the A element in a compound and the energy after the normalization of elemental A. $E(B)$, $E(C)$, b and c are identical. To evaluate the anodic catalytic performance, the following formula can interpret the adsorption property value:

$$E_{ads} = E_{sur-H_2} - E_{sur} - E_{H_2} \quad (2)$$

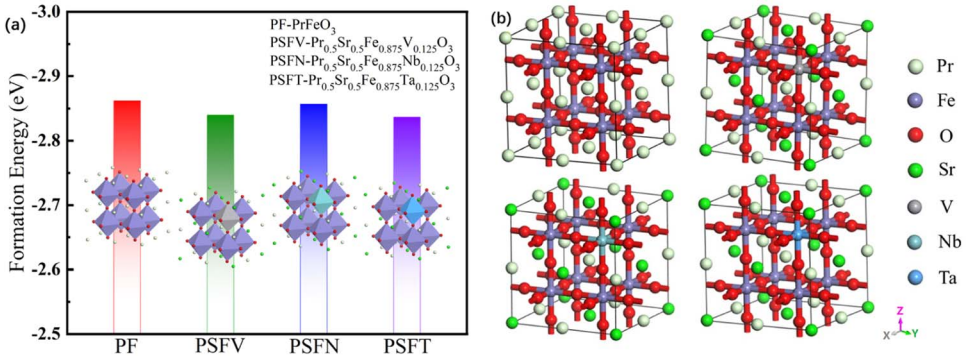

Fig. 1 (a) The formation energy and (b) the optimized model of the $PrFeO_{3-\delta}$, $Pr_{0.5}Sr_{0.5}Fe_{0.875}V_{0.125}O_{3-\delta}$, $Pr_{0.5}Sr_{0.5}Fe_{0.875}Nb_{0.125}O_{3-\delta}$ and $Pr_{0.5}Sr_{0.5}Fe_{0.875}Ta_{0.125}O_{3-\delta}$ bulk materials.

where E_{sur-H_2} and E_{sur} are the adsorption structure energy and the surface structure energy, respectively. E_{H_2} is the energy of hydrogen.

3. Results and discussion

3.1. $PrFeO_{3-\delta}$ bulk materials of pristine and co-doped

3.1.1. Bulk stability. The optimized pristine and co-doped $PrFeO_{3-\delta}$ bulk systems are shown in Fig. 1. The pristine and co-doped $PrFeO_{3-\delta}$ shows a perovskite structure, which is consistent with the previous theoretical result.[54] The H–H bond distance obtained from GGA calculations is 0.750 Å, which is inosculated with the experimental measurement.[63] Excellent stability is maintained by the $Pr_{0.5}Sr_{0.5}Fe_{0.875}Nb_{0.125}O_{3-\delta}$ of the co-doped systems.

The oxygen vacancy formation energy of the pristine $PrFeO_{3-\delta}$ is shown in Fig. 2. The para-0.083 oxygen vacancy concentration has the most stable structure of the $PrFeO_{3-\delta}$ with −1.799 eV formation energy. The $PrFeO_{3-\delta}$ with oxygen vacancy still shows a perovskite structure, which has no lattice distortion. The increase in oxygen vacancy can improve the $PrFeO_{3-\delta}$ anode stability.

3.1.2. Electronic properties. The pristine and co-doped $PrFeO_{3-\delta}$ band structure is displayed in Fig. 3. The indirect band gap (0.110 eV) of the $PrFeO_{3-\delta}$ goes to a semiconductor state. The excited electrons need to undergo a secondary transition to the conduction band from the valence band transition. Meanwhile, the semiconductor characteristics of the indirect band gap are maintained by the $Pr_{0.5}Sr_{0.5}Fe_{0.875}Nb_{0.125}O_{3-\delta}$, but the band gap change to 0.238 eV. The $Pr_{0.5}Sr_{0.5}Fe_{0.875}V_{0.125}O_{3-\delta}$ and $Pr_{0.5}Sr_{0.5}Fe_{0.875}Ta_{0.125}O_{3-\delta}$ are going to direct band gap materials. The band degeneracy of the $Pr_{0.5}Sr_{0.5}Fe_{0.875}V_{0.125}O_{3-\delta}$, $Pr_{0.5}Sr_{0.5}Fe_{0.875}Nb_{0.125}O_{3-\delta}$ and $Pr_{0.5}Sr_{0.5}Fe_{0.875}Ta_{0.125}O_{3-\delta}$ all are enhanced.

3.2. Pristine and co-doped $PrFeO_{3-\delta}$ (001) surface materials

3.2.1. Catalytic properties. To study the anode catalytic properties of the $PrFeO_{3-\delta}$ with the pristine and co-doping, the adsorption energy of the pristine and co-doped $PrFeO_{3-\delta}$ (001) is calculated. The principle of anode catalysis is defined as:

$$O^{2-} + H_2 \rightarrow H_2O + 2e^- \quad (3)$$

It can be seen that the premise of the pristine and co-doped $PrFeO_{3-\delta}$ catalytic reaction is hydrogen adsorption on the surface of the anode materials. According to the different adsorption sites of the same perovskite structure, the adsorption energy of the optimal adsorption site was calculated. After determining the optimal adsorption site of the same material,

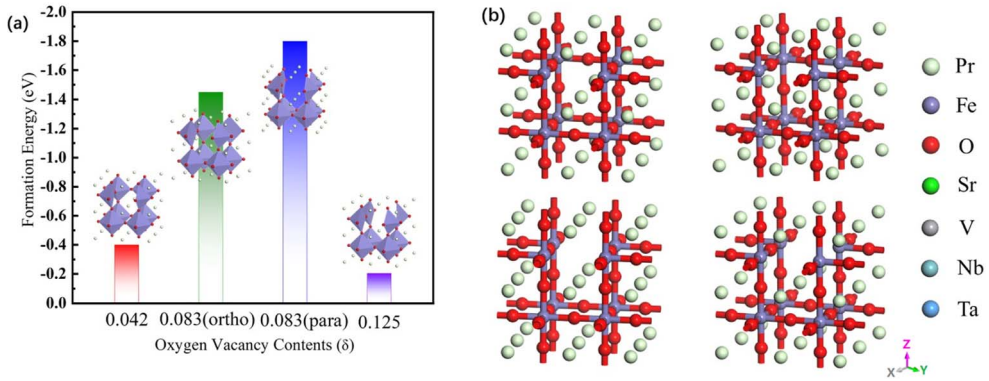

Fig. 2 (a) The oxygen vacancy formation energy and (b) optimized model of the $PFO_{3-0.042}$, *ortho*-$PFO_{3-0.083}$, *para*-$PFO_{3-0.083}$ and $PFO_{3-0.125}$ bulk materials.

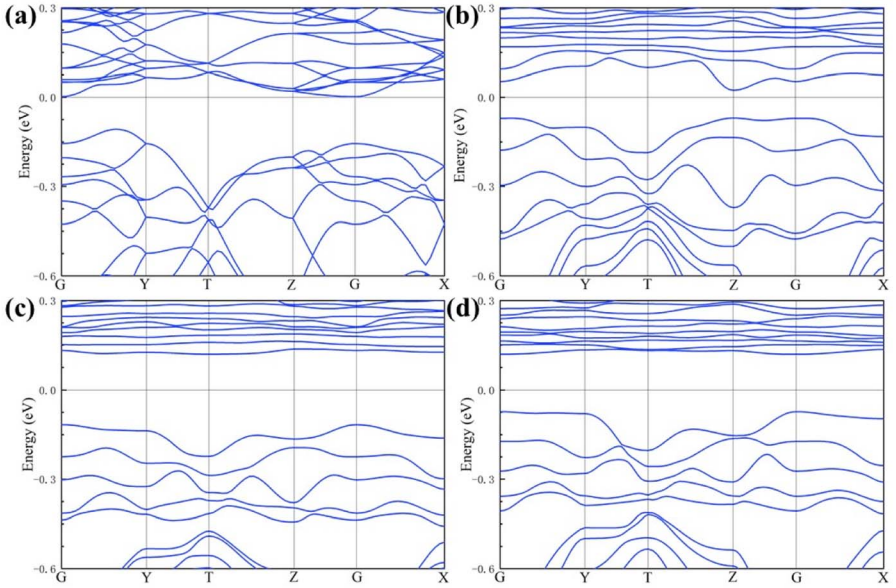

Fig. 3 Electronic structure of the (a) $PrFeO_{3-\delta}$, (b) $Pr_{0.5}Sr_{0.5}Fe_{0.875}V_{0.125}O_{3-\delta}$, (c) $Pr_{0.5}Sr_{0.5}Fe_{0.875}Nb_{0.125}O_{3-\delta}$ and (d) $Pr_{0.5}Sr_{0.5}Fe_{0.875}Ta_{0.125}O_{3-\delta}$ bulk materials.

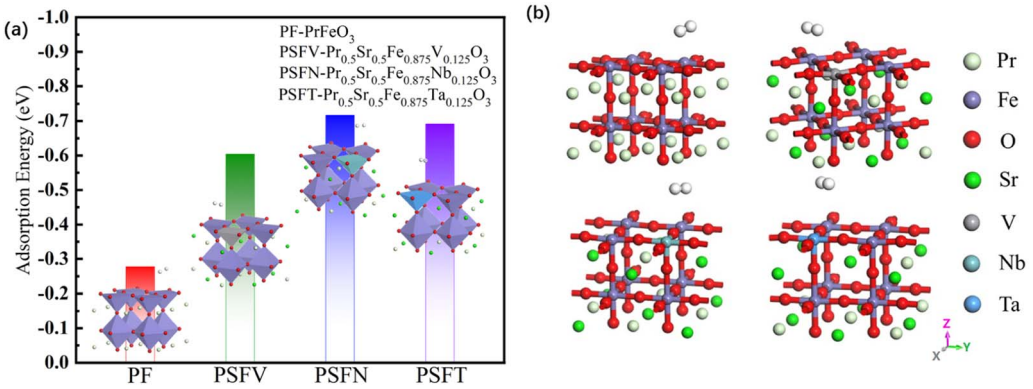

Fig. 4 (a) The adsorption energy and (b) the optimum adsorption model of the $PrFeO_{3-\delta}$, $Pr_{0.5}Sr_{0.5}Fe_{0.875}V_{0.125}O_{3-\delta}$, $Pr_{0.5}Sr_{0.5}Fe_{0.875}Nb_{0.125}O_{3-\delta}$ and $Pr_{0.5}Sr_{0.5}Fe_{0.875}Ta_{0.125}O_{3-\delta}$ surface materials.

the adsorption energy of hydrogen at the optimal site of different materials was compared to interpret the catalytic effect of anode materials.

The adsorption energy value of the pristine $PrFeO_{3-\delta}$ is −0.278 eV, much lower than the adsorption energy of chemisorption, which is judged as physical adsorption. Therefore, the adsorption energy value was tuned *via* co-doping. The adsorption energy of the pristine and co-doped $PrFeO_{3-\delta}$ (001) is shown in Fig. 4. All three kinds of Sr and V, Nb, Ta co-doped give rise to an enhancement in $PrFeO_{3-\delta}$ (001) hydrogen adsorption.

The best adsorption sites of the pristine and co-doped $PrFeO_{3-\delta}$ (001) are all directly above the iron atom. The adsorption energy value of $Pr_{0.5}Sr_{0.5}Fe_{0.875}Nb_{0.125}O_{3-\delta}$ (001) increased to −0.717, which was more obvious than that of $Pr_{0.5}Sr_{0.5}Fe_{0.875}V_{0.125}O_{3-\delta}$ and $Pr_{0.5}Sr_{0.5}Fe_{0.875}Ta_{0.125}$ $O_{3-\delta}$ (001). After adsorption, the bond lengths of H–H bonds on the surfaces of the pristine and (Sr and V, Nb, Ta) co-doped surface (001) were 0.751 Å, 0.754 Å, 0.760 Å and 0.0.756 Å, respectively, indicating that the H–H bonds were gradually elongated after adsorption occurred. With the most obvious effect for Nb. The distances between the hydrogen molecules and the surfaces of the pristine and Sr and V, Nb, Ta co-doped were 2.126 Å, 2.070 Å, 2.063 Å and 2.067 Å respectively, while the bond lengths of Fe–O bonds on the surfaces of the pristine and Sr and V, Nb, Ta co-doped were 1.881 Å, 1.936 Å, 1.985 Å and 1.961 Å respectively. The comparison shows that the adsorption of hydrogen on the pristine (001) is closer to physical adsorption, while the surfaces of Sr and V, Nb, Ta co-doped belong to chemisorption.

3.2.2. Charge transfer condition. To study the charge transfer status of the pristine and Sr and V, Nb, Ta co-doped surfaces, the differential charge density is calculated, which is defined as:

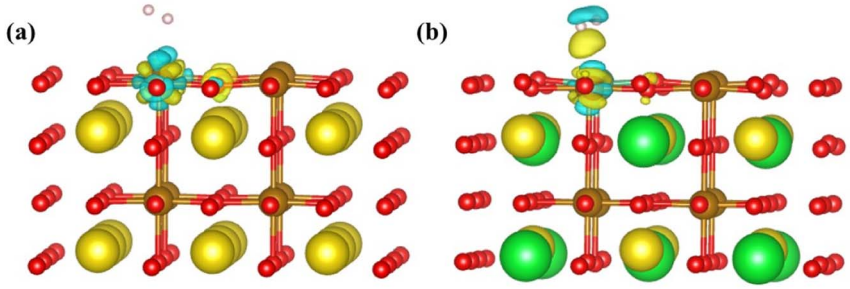

Fig. 5 The differential charge density of the (a) $PrFeO_{3-\delta}$ and (b) $Pr_{0.5}Sr_{0.5}Fe_{0.875}Nb_{0.125}O_{3-\delta}$ surface materials.

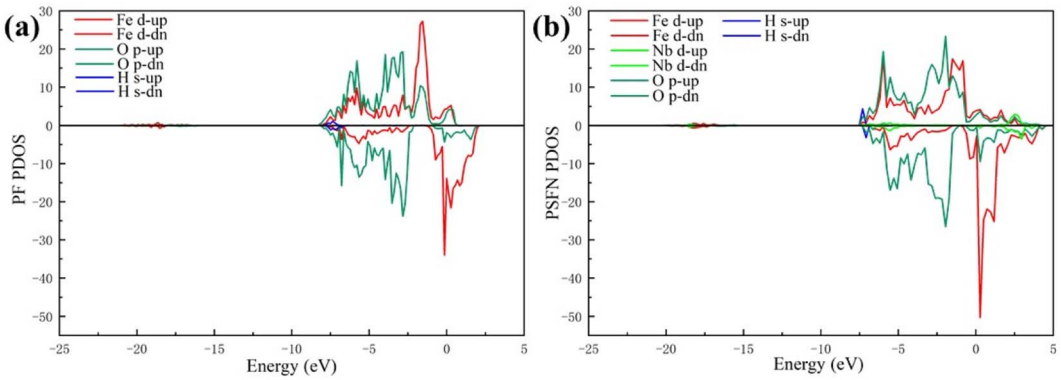

Fig. 6 The PDOS of the (a) $PrFeO_{3-\delta}$ and (b) $Pr_{0.5}Sr_{0.5}Fe_{0.875}Nb_{0.125}O_{3-\delta}$ surface materials.

$$\Delta\rho = \rho_{sur-H_2} - \rho_{sur} - \rho_{H_2} \quad (4)$$

where ρ_{sur-H_2} and ρ_{sur} are the adsorption structure and the surface structure charge density, respectively. ρ_{H_2} is the charge density of hydrogen. Yellow and cyan indicate the strengthening and weakening of electron clouds, respectively. Fig. 5 displays that the hydrogen has virtually no electron transfer to the $PrFeO_{3-\delta}$ surface (001). In stark contrast to it, the hydrogen has apparent electron transfer to $Pr_{0.5}Sr_{0.5}Fe_{0.875}Nb_{0.125}O_{3-\delta}$ (001). The two hydrogen atoms lost electrons inside, while the hydrogen molecules and the surface accumulated electrons, demonstrating that the electrons show a clear tendency to transfer from the fuel gas to the Nb Atom (directly below adsorbed gas), through the O atoms (next to the Nb atom) and finally to anode surface, which is consistent with the adsorption performance we discussed earlier.

3.2.3. D-Band center PDOS. The coupling between the d-band of perovskite oxide and the fuel gas band forms a bonding level with an energy lower than hydrogen and an anti-bonding band with an energy higher than the d orbital on the surface of perovskite. The greater the energy band higher than the Fermi level, the more stable hydrogen and perovskite surface bonding. The d-band PDOS of the $PrFeO_{3-\delta}$ and $Pr_{0.5}Sr_{0.5}Fe_{0.875}Nb_{0.125}O_{3-\delta}$ (001) is shown in Fig. 6. Relative to the $PrFeO_{3-\delta}$, the Fe, O, Pr and Nb elements of $Pr_{0.5}Sr_{0.5}Fe_{0.875}Nb_{0.125}O_{3-\delta}$ (001) all have an obvious upward shift in the d-band center.

Our works on the PDOS show that the Sr and Nb co-doping not only has an obvious d-band center upward shift but also has a narrowing of band gap due to sparse surface arrangement. Therefore, Sr and Nb can effectively enhance the chemisorption bonding performance of the anode.

3.3. Co-doped $PrFeO_{3-\delta}$ absorption final-state

As recounted in Fig. 7. The final-state of the hydrogen adsorption $Pr_{0.5}Sr_{0.5}Fe_{0.875}Nb_{0.125}O_{3-\delta}$ (001) surface has six final adsorption sites, which fixes a hydrogen atom above one iron to adjust the site of another hydrogen atom. The adsorption energies of the two broken H-atoms simultaneously adsorbed on the surface of final-

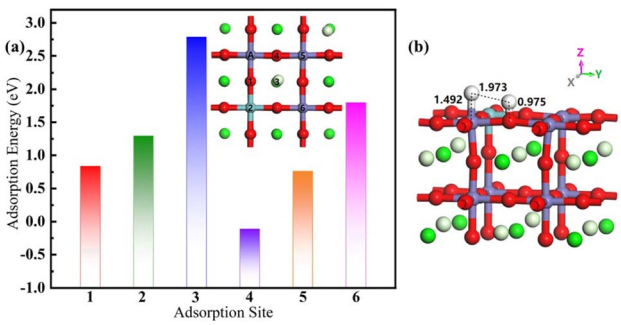

Fig. 7 (a) The adsorption energy with different position and (b) the optimal adsorption site structure of the final-state $Pr_{0.5}Sr_{0.5}Fe_{0.875}Nb_{0.125}O_{3-\delta}$ surface materials.

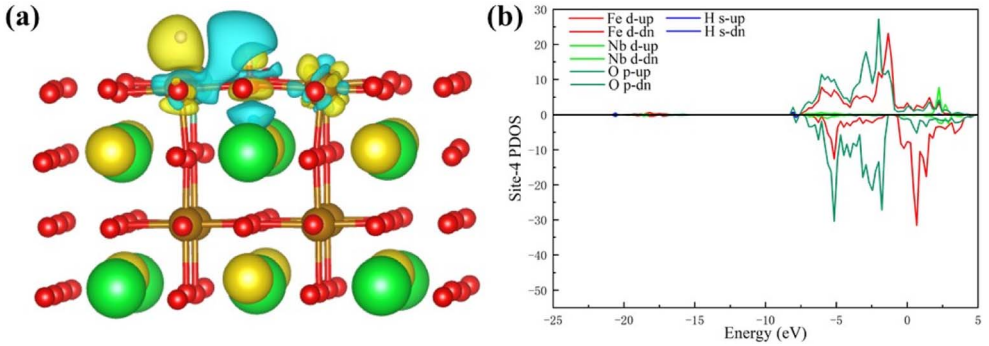

Fig. 8 (a) The differential charge density and (b) the PDOS of the final-state $Pr_{0.5}Sr_{0.5}Fe_{0.875}Nb_{0.125}O_{3-\delta}$ surface materials.

state surfaces at various points are 0.839 eV, 1.292 eV, 2.788 eV, −0.110 eV, 0.764 eV and 1.796 eV respectively. In contrast, the most stable state of the final-state adsorption surface is reached at the fourth surface model. After the gas is adsorbed onto the surface, the next step in the catalytic reaction involves the cleavage of the H–H bond. One of the H atoms positioned directly above the Nb atom undergoes a localized displacement, while the other H atom migrates to the O atom located adjacent to the Nb atom. The distances of the two hydrogen atoms from the surface are 1.492 Å and 0.975 Å, respectively, indicating that the hydrogen atom is further chemisorbed to the oxygen on the surface. At the same time, the distance between the two hydrogen atoms is stretched to 1.973 Å, indicating that this process facilitates further co-doped anodic catalysis.

To study the charge transfer status of the final-state of $Pr_{0.5}Sr_{0.5}Fe_{0.875}Nb_{0.125}O_{3-\delta}$ (001), the differential charge density of the final-state adsorption structure is shown in Fig. 8(a). This indicates that a substantial loss of electrons occurs between the two hydrogen atoms, while each hydrogen atom gains some electrons from the adjacent iron and oxygen atoms on the surface. The electrons then transfer from the two hydrogen atoms to the corresponding positions below them on the specifical site (the Nb and O atoms). Notably, the charge transferred to the surface *via* the Nb atom is greater than that transferred through the O atom after the H–H bond is broken. This observation implies that the charge distribution among the two hydrogen atoms is not uniform following the bond cleavage.

Fig. 8(b) displays the d-band PDOS of the final-state $Pr_{0.5}Sr_{0.5}Fe_{0.875}Nb_{0.125}O_{3-\delta}$ (001). Relative to the initial-state $Pr_{0.5}Sr_{0.5}Fe_{0.875}Nb_{0.125}O_{3-\delta}$ (001), the final-state $Pr_{0.5}Sr_{0.5}Fe_{0.875}Nb_{0.125}O_{3-\delta}$ (001) have an obvious upward shift in the d-band center.

Our work on the PDOS shows that the reaction mechanism for $Pr_{0.5}Sr_{0.5}Fe_{0.875}Nb_{0.125}O_{3-\delta}$ is the gradual elongation of the H–H bond until it breaks, eventually forming final-state adsorption. Therefore, the final-state is conducive to the further catalytic reaction of the $Pr_{0.5}Sr_{0.5}Fe_{0.875}Nb_{0.125}O_{3-\delta}$ anode.

4. Conclusions

To summarize, using the software package of VASP calculation works, we integrally simulated the bulk pristine and co-doped $PrFeO_{3-\delta}$, pristine and co-doped $PrFeO_{3-\delta}$ surface and final-state adsorption surface. The simulation conclusion of our DFT results shows that $Pr_{0.5}Sr_{0.5}Fe_{0.875}Nb_{0.125}O_{3-\delta}$ has suitable adsorption energy value (−0.717 eV) for anodic catalytic reaction, and in the final-state, both hydrogen atoms have charge transfer with the surface, which promotes the next step of electrode reaction. Meanwhile, the apparent charge transfer and the d-band center upward shift of the co-doped adsorption model leads to a significant enhancement in the anode catalytic degree in the SOFC reaction. Thus, the $Pr_{0.5}Sr_{0.5}Fe_{0.875}Nb_{0.125}O_{3-\delta}$ is a promising SOFC anode catalyst. In addition, the oxygen vacancy concentration at para-8.3% is the most stable state of the $PrFeO_{3-\delta}$, that are greatly affected the stability of the perovskite anode structure. Furthermore, the obtained simulation conclusions indicate that as an anode with both catalytic and stable properties, its catalytic mechanism is that hydrogen is adsorbed to the $Pr_{0.5}Sr_{0.5}Fe_{0.875}Nb_{0.125}O_{3-\delta}$ (001), the H–H bond is gradually elongated, and a new adsorption site is finally formed. Our theoretical work shows that Sr and Nb co-doping can effectively enhance the anode catalytic performance.

Conflicts of interest

The authors declare no conflicts of interest.

Acknowledgements

The authors acknowledge the support of the National Natural Science Foundation of China (Grant No. 51872067).

References

1 S. P. S. Badwal and K. Foger, *Ceram. Int.*, 1996, **22**, 257–265.
2 H. Yokokawa, N. Sakai, T. Horita, K. Yamaji and M. E. Brito, *MRS Bull.*, 2005, **30**, 591–595.
3 J. Liu, M. Yang, B. S. Chauhan, M. Abdrabboh, M. Fayed, H. Ayed, A. Mouldi, Y. Chen and X. Chen, *Process Saf. Environ. Prot.*, 2023, **175**, 783–795.
4 Y. Gao, X. Huang, M. Yuan, J. Gao, Z. Wang, Z. Lv, L. Xu and B. Wei, *J. Eur. Ceram. Soc.*, 2023, **43**, 2002–2012.
5 X. Wang and R. Hou, *Int. J. Hydrogen Energy*, 2023, S0360319923020268.
6 D. Yu, J. Hu, W. Wang and B. Gu, *Fuel*, 2023, **333**, 126442.

7 I. Ismael, A. A. El-Fergany, E. A. Gouda and M. F. Kotb, *Int. J. Hydrogen Energy*, 2023, S0360319923034183.
8 Y. Hu, C. Han, W. Li, Q. Hu and H. Wu, *Fuel Process. Technol.*, 2023, **250**, 107919.
9 A. Ding, H. Sun, S. Zhang, X. Dai, Y. Pan, X. Zhang, E. Rahman and J. Guo, *Energy Convers. Manage.*, 2023, **291**, 117327.
10 P. W. Li and M. K. Chyu, *J. Heat Transfer*, 2005, **127**, 1344–1362.
11 P. Boldrin and N. P. Brandon, *Nat. Catal.*, 2019, **2**, 571–577.
12 H.-H. Möbius, *J. Solid State Electrochem.*, 1997, **1**, 2–16.
13 P. Sarkar, L. Yamarte, H. Rho and L. Johanson, *Int. J. Appl. Ceram. Technol.*, 2007, **4**, 103–108.
14 J. Koh, *Solid State Ionics*, 2002, **149**, 157–166.
15 F. Wang, W. Wang, J. Qu, Y. Zhong, M. O. Tade and Z. Shao, *Environ. Sci. Technol.*, 2014, **48**, 12427–12434.
16 M. Pihlatie, A. Kaiser and M. Mogensen, *Solid State Ionics*, 2009, **180**, 1100–1112.
17 Y. Yao, C. Shi, Z. Huang, P. Cai and S. Wang, *J. Power Sources*, 2022, **521**, 230905.
18 M. Y. Cheng and B. J. Hwang, *J. Am. Chem. Soc.*, 2004, **2**, 49.
19 O. Costa-Nunes, R. J. Gorte and J. M. Vohs, *J. Power Sources*, 2005, **141**, 241–249.
20 S. Jung, C. Lu, H. He, K. Ahn, R. J. Gorte and J. M. Vohs, *J. Power Sources*, 2006, **154**, 42–50.
21 X.-F. Ye, B. Huang, S. R. Wang, Z. R. Wang, L. Xiong and T. L. Wen, *J. Power Sources*, 2007, **164**, 203–209.
22 X. Xiong, J. Yu, X. Huang, D. Zou, Y. Song, M. Xu, R. Ran, W. Wang, W. Zhou and Z. Shao, *J. Mater. Sci. Technol.*, 2022, **125**, 51–58.
23 S. Pang, G. Yang, Y. Su, J. Xu, X. Shen, M. Zhu, X. Wu, S. Li and C. Chen, *Ceram. Int.*, 2019, **45**, 14602–14607.
24 Q. Zhou, T. Zhang, C. Zhao, L. Qu, Y. He, T. Wei and X. Tong, *Mater. Res. Bull.*, 2020, **131**, 110986.
25 C.-Y. Gu, X.-S. Wu, J.-F. Cao, J. Hou, L.-N. Miao, Y.-P. Xia, C. Fu and W. Liu, *Int. J. Hydrogen Energy*, 2020, **45**, 23422–23432.
26 X. Meng, G. Long, S. Liu, Y. Ji, M. Pang, B. Wang, S. Lü and J. Yang, *Int. J. Hydrogen Energy*, 2015, **40**, 6935–6941.
27 X. Zhang, L. Zhang, J. Meng, W. Zhang, F. Meng, X. Liu and J. Meng, *Int. J. Hydrogen Energy*, 2017, **42**, 29498–29510.
28 S. B. Adler, *Chem. Rev.*, 2004, **104**, 4791–4844.
29 Y. Gao, X. Huang, M. Yuan, J. Gao, Z. Wang, A. M. Abdalla, A. K. Azad, L. Xu, Z. Lv and B. Wei, *J. Power Sources*, 2022, **540**, 231661.
30 Y. Gao, X. Huang, Z. Wang, M. Yuan, J. Gao, Z. Lv, L. Xu and B. Wei, *Int. J. Hydrogen Energy*, 2023, **48**, 2341–2350.
31 S. Yu, Y. Li, Y. Wang, Y. Yin and Q. Zhang, *Ceram. Int.*, 2023, **49**, 30905–30913.
32 J. H. Kuo, H. U. Anderson and D. M. Sparlin, *J. Solid State Chem.*, 1990, **87**, 55–63.
33 Z. Shao and S. M. Haile, *Nature*, 2004, **431**, 170–173.
34 Y. Yang, X. Su, S. Pan and Z. Yang, *Phys. Chem. Chem. Phys.*, 2015, **17**, 26359–26368.
35 C.-Y. Liu, S.-Y. Tsai, C.-T. Ni, K.-Z. Fung and C.-Y. Cho, *Jpn. J. Appl. Phys.*, 2019, **58**, SDDG03.
36 F. Zhao, C. Jin, C. Yang, S. Wang and F. Chen, *J. Power Sources*, 2011, **196**, 688–691.
37 K. Deshpande, A. Mukasyan and A. Varma, *J. Power Sources*, 2006, **158**, 60–68.
38 T. S. Li, M. Xu, C. Gao, B. Wang, X. Liu, B. Li and W. G. Wang, *J. Power Sources*, 2014, **258**, 1–4.
39 H. Y. Chang, Y. M. Wang, C. H. Lin and S. Y. Cheng, *Acad. Manag. Rev.*, 2013, **702**, 111–114.
40 B. Huang, S. R. Wang, R. Z. Liu, X. F. Ye, H. W. Nie, X. F. Sun and T. L. Wen, *J. Power Sources*, 2007, **167**, 39–46.
41 I. Z. Rahman, M. A. Raza and M. A. Rahman, *Acad. Manag. Rev.*, 2012, **445**, 497–502.
42 B. A. Boukamp, *Nat. Mater.*, 2003, **2**, 294–296.
43 W. Y. Hernández, M. A. Centeno, F. Romero-Sarria and J. A. Odriozola, *J. Phys. Chem. C*, 2009, **113**, 5629–5635.
44 W. Cai, M. Zhou, D. Cao, X. Yan, Q. Li, S. Lü, C. Mao, Y. Li, Y. Xie, C. Zhao, J. Yu, M. Ni, J. Liu and H. Wang, *Int. J. Hydrogen Energy*, 2020, **45**, 21873–21880.
45 Y. Li, Z. Wang, J. Li, X. Zhu, Y. Zhang, X. Huang, Y. Zhou, L. Zhu and Z. Lü, *J. Alloys Compd.*, 2017, **698**, 794–799.
46 Y. Tao, Y. Zhou, W. Li, J. Shao, L. Bai and X. Liu, *J. Alloys Compd.*, 2018, **741**, 1091–1097.
47 S. Wang, Y. Wu, Y. Gao, H. Chen, A. M. Abdalla, A. K. Azad, Z. Lü and B. Wei, *Int. J. Hydrogen Energy*, 2022, **47**, 34205–34215.
48 S. Wang, Y. Wu, H. Chen, Y. Gao, J. Liu, M. Li, Z. Lü and B. Wei, *J. Alloys Compd.*, 2023, **932**, 167685.
49 X. Luo, G. Wang, Y. Huang, B. Wang, H. Yuan and H. Chen, *J. Phys. Chem. C*, 2017, **121**, 18534–18543.
50 S. P. Jiang, L. Liu, K. P. Ong, P. Wu, J. Li and J. Pu, *J. Power Sources*, 2008, **176**, 82–89.
51 Y. Shin, K.-Y. Doh, S. H. Kim, J. H. Lee, H. Bae, S.-J. Song and D. Lee, *J. Mater. Chem. A*, 2020, **8**, 4784–4789.
52 Y. Zhou, Z. Lü, B. Wei, Z. Wang and X. Zhu, *Solid State Commun.*, 2015, **201**, 31–35.
53 Y. Zhou, Z. Lü, P. Guo, Y. Tian, X. Huang and W. Su, *Appl. Surf. Sci.*, 2012, **258**, 2602–2606.
54 M. Rezaiguia, W. Benstaali, A. Abbad, S. Bentata and B. Bouhafs, *J. Supercond. Novel Magn.*, 2017, **30**, 2581–2590.
55 G. Kresse and J. Furthmüller, *Phys. Rev. B: Condens. Matter Mater. Phys.*, 1996, **54**, 11169–11186.
56 G. Kresse and D. Joubert, *Phys. Rev. B: Condens. Matter Mater. Phys.*, 1999, **59**, 1758–1775.
57 G. Kresse and J. Hafner, *Phys. Rev. B: Condens. Matter Mater. Phys.*, 1993, **47**, 558–561.
58 M. Ernzerhof and G. E. Scuseria, *J. Chem. Phys.*, 1999, **110**, 5029–5036.
59 J. A. White and D. M. Bird, *Phys. Rev. B: Condens. Matter Mater. Phys.*, 1994, **50**, 4954–4957.
60 I. V. Solovyev, P. H. Dederichs and V. I. Anisimov, *Phys. Rev. B: Condens. Matter Mater. Phys.*, 1994, **50**, 0163–1829.
61 Y. W. Suen, *Phys. Rev. B: Condens. Matter Mater. Phys.*, 1994, **50**, 0163–1829.
62 H. J. Kulik, M. Cococcioni, D. A. Scherlis and N. Marzari, *Phys. Rev. Lett.*, 2006, **97**, 0031–9007.
63 W. Mikenda, *J. Mol. Struct.*, 1986, **147**, 1–15.